*American Mineralogist, Volume 89, pages 1367–1373, 2004*

# Behavior of cation vacancy in kenotetrahedral Cr-spinels from Albanian eastern belt ophiolites

**FERDINANDO BOSI,* GIOVANNI B. ANDREOZZI, VINCENZO FERRINI, AND SERGIO LUCCHESI**

Dipartimento di Scienze della Terra, Università di Roma "La Sapienza", P.le A.Moro 5, 00185 Roma, Italy

## ABSTRACT

The crystal chemistry of 17 Cr-spinels from the Albanian eastern belt ophiolites was studied by a multi-analytical approach (EMPA, MS, SREF), processing the data with a tested optimization model to obtain site populations. The samples come from the three most important ultramafic massifs of Albania (Tropoja, Bulqiza, and Shebenik), and occur in ultramafic cumulates as well as in ultramafic mantle tectonites, associated with serpentinized olivine. All samples are characterized by Cr ↔ Al and minor Mg ↔ $Fe^{2+}$ substitutions, and may be classified as magnesiochromite, except one, which is spinel s.s. Cation distributions showed that Cr and Al are ordered in M, and $Fe^{2+}$ and Mg in the T site. Contents of $Fe^{3+}$ measured by MS were always higher than those calculated from EMPA, and this non-stoichiometry reveals that the Albanian crystals underwent an increase in $f_{O_2}$ conditions after mineral formation. Cation vacancies produced by $Fe^{2+}$ oxidation occur in the T site, and the oxidation mechanism, is described by:

$$2\ {}^{T}Fe^{2+} + \tfrac{1}{2}\ O_2 \rightarrow 2\ {}^{T}Fe^{3+} + O^{2-} + {}^{T}\square.$$

T-O variations show a non-linear regression with ${}^{T}Fe^{2+}$, and this trend is due to both the cooperative effects of ${}^{T}Mg \leftrightarrow {}^{T}Fe^{2+}$ substitution and ${}^{T}Fe^{2+}$ oxidation. Cation vacancy in the T site does not impart rigidity to the polyhedron, because it cannot have chemical bonds with ligands: this feature, together with the spinel topology, makes the tetrahedron adopt "soft" behavior. In effect, the ${}^{T}\square$-O distance does not have a single value, but changes according to the population of the M site, as confirmed by comparison with literature data and also by application of the Bond Valence Model.

## INTRODUCTION

Spinels are found in a wide range of geological environments, from upper mantle to crust, crystallizing in various physico-chemical conditions. Their importance as petrogenetic indicators and for oxygen thermobarometry has been widely recognized and has prompted extensive studies (e.g., Sack and Ghiorso 1991). In particular, most studies have focused on intracrystalline order-disorder relationships and their dependence on spinel composition, equilibrium temperature, and cooling history (e.g., O'Neill and Navrotsky 1983, 1984; Nell and Wood 1989; Wood 1990; O'Neill and Dollase 1994). The oxygen thermobarometry of abyssal peridotites reveals that they are substantially more reduced than continental peridotites, the former having an average $f_{O_2}$ of ca. 1 log unit below Fayalite-Magnetite-Quartz (FMQ) solid buffer (Wood 1991). Upper-mantle oxygen fugacity has been investigated by different approaches, and very good results have been obtained by exploiting mineral equilibria in spinel-bearing ultramafic rocks (O'Neill and Wall 1987; Mattioli and Wood 1988). The determination of $Fe_3O_4$ content of mantle xenoliths was shown to be the key factor in obtaining accurate $f_{O_2}$ estimations (Wood and Virgo 1989). The latter authors used Mössbauer spectroscopy to measure $Fe^{2+}/Fe^{3+}$ ratios of spinels, because conventional microprobe techniques are fairly precise, but not accurate enough, with errors of ±3 mol% $Fe_3O_4$, which corresponds to an uncertainty in $f_{O_2}$ of 4.5 log units. However, because thermodynamic models for $f_{O_2}$ estimation may be affected significantly by spinel non-stoichiometry (Mattioli and Wood 1988; Herd and Papike 1999), full topochemical characterization of spinels is crucial before using them for oxygen thermobarometry.

From the spinel structural formula, ${}^{IV}(A_{1-i}B_i)^{VI}(A_iB_{2-i})O_4$, two extreme cation configurations are possible: normal ($i = 0$) and inverse ($i = 1$). The *Fd*3*m* structure may be described fully by two variables: lattice parameter ($a$) and oxygen fractional coordinate ($u$), which are simple functions of tetrahedral (T) and octahedral (M) bond distances (Hill et al. 1979). When the T-site population is constant, $u$ is inversely proportional to M-O. Any departure from linearity is due to structural dragging of the second coordination sphere: e.g., change of tetrahedral cation-to-oxygen bond distances due to ${}^{M}Fe^{3+}$, ${}^{M}Ni^{2+}$ and ${}^{M}V^{3+}$ (Lavina et al. 2002, 2003).

In the $(Mg,Fe^{2+})(Al,Fe^{3+},Cr^{3+})_2O_4$ system, Mg, Fe, and Al are disordered between T and M sites, whereas $Cr^{3+}$ is ordered in the M site, because of its octahedral site preference energy (O'Neill and Navrotsky 1984). This marked preference of $Cr^{3+}$ for the octahedral environment strongly influences spinel topochemistry, by affecting the site distribution of the other cations (Martignago et al. 2003). The similar behavior was recently highlighted also in the $(Mg,Zn)(Al,Fe)_2O_4$ system, due to the strong preference of Zn for the tetrahedral environment (Andreozzi et al. 2001).

In this paper, the crystal chemistry of Cr-spinels from the Albanian eastern belt ophiolites was studied by a multi-analytical approach, processing the data with a tested optimization model for site populations.

* E-mail: ferdinando.bosi@uniroma1.it

## GEOLOGICAL SETTING

The chromite samples come from the three most important ultramafic massifs belonging to the eastern belt ophiolites of Albania: Tropoja, Bulqiza, and Shebenik. The Tropoja massif, located in the northern part of Albania, is about 4000–6000 m thick, and includes a mantle harzburgite-dunite sequence, a dunite-harzburgite transitional zone, and an ultramafic cumulate sequence (Mekshiqi et al. 1998). Chromite ore deposits, occurring from a depth of 300 m, have been disrupted extensively by tectonics and belong to: (a) dunite bands and lenses embedded in tectonitic harzburgite, (b) dunite of the cumulate sequence. The Bulqiza massif, located in central Albania, contains the largest number of chromite ore deposits and is mainly composed of a mantle sequence topped by a mafic-ultramafic cumulate sequence. The mantle sequence is made up of harzburgite with dunite lenses, the latter increasing in abundance in the upper part of the massif and from E to W. The cumulate sequence contains dunite and, rarely, plagioclase-bearing dunite, lherzolite, and wehrlite. The abundant chromite occurs in layers, pods, and lenses, always associated with a dunitic envelope, both in the lower dunitic portion of the cumulate sequence and within mantle harzburgites (Beccaluva et al. 1998). Chromite from Bulqiza, which shows the highest Cr contents with respect to the other Albanian deposits, was generated during gravitative differentiation processes, and may be considered as due to early crystallization from a basaltic magma generated by partial melting in the upper mantle (Dobi et al. 1998). The Shebenik massif, located in southern Albania, is one of the least investigated from the viewpoint of prospecting. Its thickness is about 4000 m, and the chromite bodies discovered so far lie at a depth of 300 m. Based on known petrographic and structural features, the Shebenik massif does not show particular differences with respect to the others.

In these massifs, chromite occurs in ultramafic cumulates as well as in ultramafic mantle tectonites, associated with olivine. According to the genetic model proposed by Beccaluva et al. (1998), chromite and olivine directly crystallized from low-Ti picritic basalt parental magma, generated deep in the mantle in an intraoceanic suprasubduction tectonic setting. Temperatures retrieved by the olivine-spinel geothermometer are in the range 525–730 °C, which are well below temperatures found in abyssal peridotites, but typical of low-temperature, water-assisted diffusional equilibration in shallow suprasubduction mantle rocks (Beccaluva et al. 1998).

Iddingsite-type alteration was not observed in olivine, and the variable degree of serpentinization was generated by fluid circulation during tectonic uplift.

## EXPERIMENTAL METHODS

### Single-crystal structural refinement (SREF)

The examined samples constitute a set of 14 hand-picked specimens (Table 1), from which 17 crystals were extracted. For X-ray data collection, small equidimensional fragments (ca. 200 μm) of the selected Cr-spinels were mounted on a Siemens P4 automated four-circle, single-crystal diffractometer. Details of data collection are shown in Table 2.

For collection of diffraction intensity data, one-eighth of the reciprocal space was examined with the ω scan method and fixed scan range. Scan speed was variable, depending on reflection intensity, estimated with a pre-scan. Background was measured with a stationary counter and crystal at the beginning and end of each scan, in both cases for half the scan time. Three standard reflections were monitored every 47 measurements. Further details of experimental conditions may be found in Lucchesi et al. (1997).

The SHELXTL-PC program package allowed reduction of X-ray diffraction (XRD) data. Intensities were corrected for polarization and Lorentz effects. The absorption correction was accomplished with a semi-empirical method. No significant deviations from *Fd3m* symmetry were noted: the appearance of forbidden space-group reflections such as 200 was attributed, on the basis of ψ-scan checks, to double reflection (Tokonami and Horiuchi 1980). During structural refinement, variable parameters were: scale factor, oxygen coordinate, mean atomic numbers (m.a.n.) of T and M sites, displacement parameters, and isotropic secondary extinction coefficient (Table 3). The starting oxygen coordinate was that proposed by Princivalle et al. (1989). No chemical constraints were applied during refinement. Fully ionized scattering curves for all elements except oxygen (20% ionized) were used, because they proved to furnish the best values of conventional agreement factors over all $\sin\theta/\lambda$ intervals and the best coherence between observed and calculated F(222), according to Della Giusta et al. (1996). Off-diagonal displacement parameters were extremely small and of the same magnitude as their σ, when not forced to zero by symmetry; thus, only $U_{11}$ are shown in Table 3. Three isotropic, full-matrix, refinement cycles were followed by anisotropic cycles until convergence was attained. The disagreement coefficient (R) values were very satisfactory (Table 3).

### Electron microprobe analysis (EMPA)

The same crystals used for X-ray data collection were mounted on a glass slide and polished for electron microprobe analysis (WDS method) on a Cameca-Camebax instrument operating at an accelerating potential of 15 kV and a sample current of 15 nA. Synthetic phases (MgO, MnO, ZnS, NiO, $Fe_2O_3$, $Al_2O_3$, $Cr_2O_3$, $Pb_5(VO_4)_3Cl$, $Ca_2Si_2O_6$, and $TiO_2$) were used as standards. For raw data reduction, the PAP computer program was applied (Pouchou and Pichoir 1984). Each element determination was accepted after checking that the intensity of analyzed standards before and after each measurement was within 1.00 ± 0.01. Precision for major elements (Mg, Al, Fe, Cr) was usually within 1% of the actual amount present, and that of minor elements was within about 5%. Very great care was devoted to the microprobe analyses—no less than 15 point analyses were performed on each crystal. Results are shown in Table 4.

**TABLE 1.** Albanian samples

| Sample | Provenance | Sequence |
|---|---|---|
| Tro6 | Tropoja massif | cumulate |
| Tro4 | Tropoja massif | tectonite |
| Shb2 | Shebenik massif | tectonite |
| Shb4 | Shebenik massif | cumulate |
| Shkm1 | Shkalla, Bulqiza massif | tectonite |
| Shkm3 | Shkalla, Bulqiza massif | tectonite |
| Thkv1 | Thekna, Bulqiza massif | tectonite |
| Thkv2 | Thekna, Bulqiza massif | tectonite |
| N2 | Bulqize, Bulqiza massif | tectonite |
| N4 | Bulqize, Bulqiza massif | tectonite |
| N7 | Bulqize, Bulqiza massif | tectonite |
| N10 | Bulqize, Bulqiza massif | tectonite |
| Ba4 | Bater, Bulqiza massif | cumulate |
| Ba2 | Bater, Bulqiza massif | cumulate |

**TABLE 2.** Parameters for X-ray data collection

| | |
|---|---|
| **Determination of unit-cell parameters** | |
| Radiation | Mo$K\alpha_1$ (0.70930 Å) |
| Reflections used | 13 (Friedel pairs on both +2θ and –2θ) |
| Range | 85°–95° 2θ |
| Temperature | 296 K |
| **Diffraction intensity collection** | |
| Radiation | Mo$K\alpha$ (0.71073 Å) |
| Monochromator | High crystallinity graphite crystal |
| Range | 3°–95° 2θ |
| Reciprocal space range | $0 \le h, k, l \le 17$ |
| Scan method | ω |
| Scan range | 2.4° 2θ |
| Scan speed | Variable 2.93°–29.30° 2θ/min |
| Temperature | 296 K |
| **Data reduction** | |
| Refinement | SHELXTL – PC |
| Corrections | Lorentz, Polarization |
| Absorption correction | Semi-empirical, 13 ψ scans (10°–95° 2θ) |
| Set of measured reflections | 707–718 |
| Set of unique reflections | 151–169 {I > 2σ (I)} |

**TABLE 3.** Results of structural refinements

| | $a_0$ (Å) | $u$ | T-O (Å) | M-O (Å) | m.a.n. T | m.a.n. M | $U_{11}$(T) | $U_{11}$(M) | $U_{11}$(O) | Ext. | R |
|---|---|---|---|---|---|---|---|---|---|---|---|
| Tro6-f | 8.2743(8) | 0.26156(10) | 1.9571(8) | 1.9776(8) | 15.8(2) | 22.1(4) | 73(3) | 62(1) | 84(2) | 0.0062 | 2.37 |
| Tro4-f | 8.2915(5) | 0.26267(8) | 1.9771(7) | 1.9734(6) | 18.0(2) | 21.2(3) | 62(2) | 41(1) | 63(2) | 0.0041 | 1.86 |
| Tro4-j | 8.2864(7) | 0.26253(8) | 1.9739(7) | 1.9732(6) | 17.1(2) | 21.3(3) | 62(2) | 42(1) | 61(2) | 0.0042 | 1.72 |
| Shb2-m | 8.2793(7) | 0.26187(7) | 1.9627(6) | 1.9764(5) | 16.3(1) | 21.9(2) | 62(2) | 46(1) | 67(2) | 0.0046 | 1.37 |
| Shb4-b | 8.2991(3) | 0.26212(8) | 1.9710(7) | 1.9793(6) | 16.3(1) | 21.7(3) | 61(2) | 42(1) | 65(2) | 0.0042 | 1.84 |
| Shb4-f | 8.2902(8) | 0.26220(9) | 1.9701(8) | 1.9766(7) | 16.9(2) | 22.0(3) | 57(2) | 35(1) | 54(2) | 0.0035 | 2.05 |
| Shkm1-i | 8.3006(3) | 0.26224(6) | 1.9731(5) | 1.9788(5) | 16.1(1) | 21.6(2) | 65(1) | 46(1) | 66(1) | 0.0046 | 1.30 |
| Shkm3-g | 8.2982(5) | 0.26238(8) | 1.9745(7) | 1.9772(6) | 16.8(2) | 21.7(3) | 60(2) | 41(1) | 62(2) | 0.0041 | 1.69 |
| Thkv1-a | 8.3081(3) | 0.26227(10) | 1.9753(8) | 1.9803(7) | 16.9(2) | 22.0(4) | 58(2) | 39(1) | 59(2) | 0.0039 | 1.78 |
| Thkv1-w | 8.3033(3) | 0.26207(8) | 1.9713(7) | 1.9807(6) | 16.6(2) | 22.0(3) | 66(2) | 48(1) | 70(2) | 0.0048 | 1.52 |
| Thkv2-w | 8.3057(4) | 0.26225(9) | 1.9745(8) | 1.9799(7) | 16.5(2) | 22.1(3) | 57(2) | 36(1) | 57(2) | 0.0036 | 1.92 |
| N2-h | 8.3071(3) | 0.26223(9) | 1.9745(8) | 1.9804(7) | 16.7(2) | 21.9(4) | 64(2) | 43(1) | 64(2) | 0.0043 | 2.20 |
| N4-x | 8.1992(4) | 0.26315(7) | 1.9619(6) | 1.9480(5) | 15.7(1) | 17.2(4) | 64(2) | 49(1) | 70(2) | 0.0049 | 1.21 |
| N7-g | 8.3091(4) | 0.26239(7) | 1.9773(6) | 1.9797(5) | 17.2(2) | 21.9(3) | 60(2) | 39(1) | 60(2) | 0.0039 | 1.72 |
| N10-a | 8.3133(4) | 0.26236(7) | 1.9779(6) | 1.9809(5) | 17.6(2) | 22.2(3) | 64(2) | 44(1) | 61(1) | 0.0044 | 1.57 |
| Ba4-c | 8.3101(3) | 0.26213(7) | 1.9738(6) | 1.9819(5) | 16.2(2) | 22.2(3) | 65(2) | 46(1) | 66(2) | 0.0046 | 1.41 |
| Ba2-y | 8.3043(4) | 0.26187(8) | 1.9687(7) | 1.9824(6) | 15.8(2) | 22.4(3) | 61(2) | 45(1) | 65(2) | 0.0045 | 1.60 |

*Notes:* Cell origin at $\bar{3}$m; m.a.n. = mean atomic number; $U_{11}$ = displacement parameters (Å$^2 \times 10^4$), $U_{11} = U_{22} = U_{33}$ and $U_{12} = U_{13} = U_{23} = 0$ within error; Ext. = isotropic secondary extinction coefficient ($\sigma = 0.0001$); R (%) in the form : $(\Sigma|F_{obs} - F_{calc}|)/(\Sigma F_{obs})$.

## $^{57}$Fe Mössbauer spectroscopy (MS)

**Room temperature and low-temperature experimental procedures.** Cr-spinel grains were hand-picked from the 14 Albanian specimens under a binocular microscope, cleaned of surface impurities, crushed, and ground in acetone. In order to attain high-purity samples, powders were preliminarily checked by powder XRD. Results excluded the presence of extra phases. Mössbauer absorbers were prepared by pressing finely ground samples with a powdered acrylic resin (Lucite) in to self-supporting discs. Based on EMPA results, 20 mg of sample powder were used, on average, to prepare the Mössbauer absorbers. This sample amount corresponds to about 2 mg Fe/cm$^2$, and is well below the absorber density at which thickness effects seriously influence Mössbauer results. Absorbers were analyzed by $^{57}$Fe Mössbauer spectroscopy in transmission mode at both room temperature (RT) and liquid nitrogen (LN) temperature (298 and 77 K, respectively).

Spectra were collected using a conventional spectrometer system operating in constant acceleration mode with a $^{57}$Co source of nominal 1.85 GBq (50 mCi) in a rhodium matrix. LN measurements were performed using a continuous flow cryostat filled with liquid nitrogen, with temperature controlled to within ±0.2 K. In order to have good statistics, data collection time for each sample was prolonged up to three days. Spectral data for the velocity range –4 to +4 mm/s were recorded in a multichannel analyzer using 512 channels. After velocity calibration against a spectrum of high-purity α-Fe foil (25 mm thick) taken at RT, the raw data were folded to 256 channels. The spectra were fitted assuming Lorentzian line shape and using the commercial fitting program Recoil 1.04. Reduced $\chi^2$ was used as a parameter to evaluate the statistical best fit, and uncertainties were calculated using the covariance matrix. Errors are estimated at about ±0.02 mm/s for center shift (CS), quadrupole splitting (QS), and line width (Γ), and no less then ±2% for doublet areas.

**$^{57}$Fe Mössbauer spectra-fitting strategy.** Both RT and LN Mössbauer spectra are dominated by a broad, doublet-like asymmetric absorption with a complex inner part (Fig. 1). According to the existing literature, the outer part of the absorption envelope is due to $Fe^{2+}$, in tetrahedral and/or octahedral coordination (Larsson et al. 1994; Waerenborgh et al. 1994; Hålenius et al. 2002). CS values of doublet components range from 0.86 to 0.97 mm/s and from 0.99 to 1.06 mm/s at RT and LN conditions, respectively. QS values range from 0.75 to 1.73 mm/s and from 0.93 to 3.24 mm/s at RT and LN conditions, respectively. As already observed in the literature, $Fe^{2+}$ contributions are strongly temperature-dependent, i.e., at LN temperature, QS increases and the spectra are better resolved (Fig. 1). At both temperatures, doublets with high QS values can be related to $Fe^{2+}$ in tetrahedral coordination, due to next-nearest neighbor effect, i.e., the non-spherical cation distribution in the second coordination sphere of this site (Waerenborgh et al. 1990). Moreover, $Fe^{2+}$ doublets with lowest QS values may be attributed to octahedrally coordinated $Fe^{2+}$ (Larsson et al. 1994; Hålenius et al. 2002).

However, $Fe^{2+}$ contributions do not explain the large asymmetric envelope displayed by the spectra of our chromite samples. Therefore, another absorption band, contributing to the region between zero and 1 mm/s, had to be considered, and was attributed to $Fe^{3+}$. CS values of this doublet range from 0.27 to 0.41 mm/s and from 0.38 to 0.47 mm/s at RT and LN conditions, respectively. QS values range from 0.42 to 0.80 mm/s and from 0.49 to 0.85 mm/s at RT and LN conditions, respectively. To account for different values taken by recoil-free fraction for $Fe^{2+}$ and $Fe^{3+}$ ions at RT (De Grave and Van Alboom 1991), contents of $Fe^{2+}$ and $Fe^{3+}$ of our samples were obtained from doublet areas of LN spectra, and results are listed in Table 4. Full analysis of the spectra will be discussed elsewhere (work in progress).

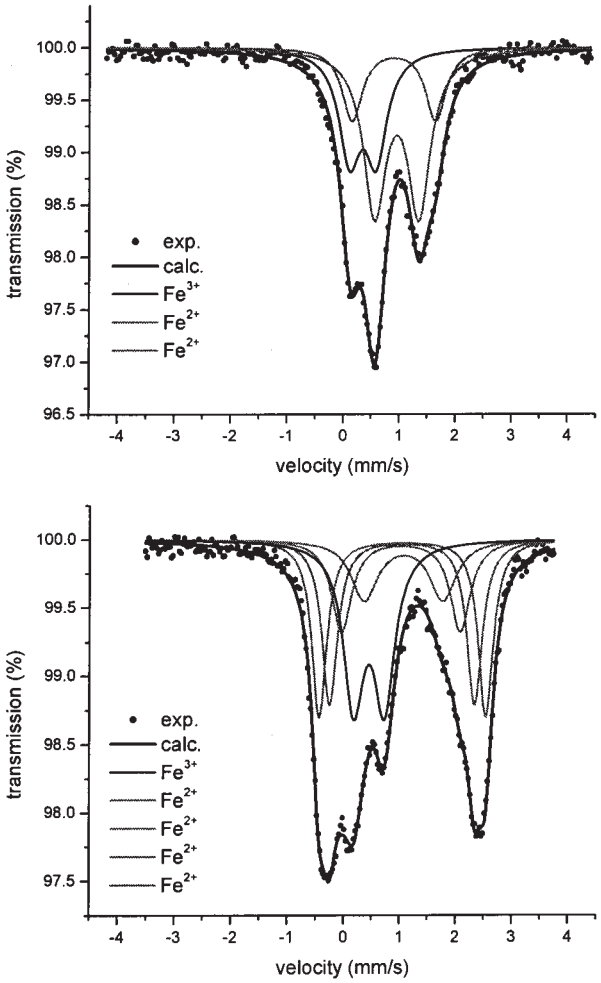


**FIGURE 1.** Typical $^{57}$Fe Mössbauer spectra of Albanian Cr-spinels collected at room temperature **(a)** and temperature of liquid nitrogen **(b)**.

## CRYSTAL CHEMISTRY

The investigated crystals are characterized by high contents of $Cr^{3+}$, which range from 1.36 to 1.61 atoms per formula units (apfu), and Mg (0.58–0.73 apfu), and may therefore be classified as magnesiochromite. The only exception was crystal N4x,

**TABLE 4.** Chemical composition (% in weight) by EMPA and MS

| | Tro6-f | Tro4-f | Tro4-j | Shb2-m | Shb4-b | Shb4-f | Shkm1-i | Shkm3-g | Thkv1-a | Thkv1-w | Thkv2-w |
|---|---|---|---|---|---|---|---|---|---|---|---|
| ZnO | – | – | – | – | – | – | – | – | – | – | 0.07(1) |
| MgO | 12.8(3) | 12.0(2) | 13.2(1) | 13.7(2) | 13.3(2) | 13.4(2) | 14.31(8) | 13.5(1) | 12.9(1) | 12.9(1) | 13.89(9) |
| $Al_2O_3$ | 10.0(1) | 14.43(8) | 15.2(1) | 10.81(6) | 10.57(8) | 11.6(1) | 11.6(1) | 11.94(7) | 9.5(2) | 9.9(1) | 9.88(3) |
| $SiO_2$ | 0.04(1) | – | – | – | – | 0.03(1) | 0.05(2) | – | – | – | 0.03(1) |
| $TiO_2$ | 0.11(2) | 0.21(1) | 0.22(2) | 0.12(2) | 0.22(2) | 0.10(2) | 0.11(1) | 0.13(2) | 0.09(2) | 0.07(1) | 0.10(3) |
| $V_2O_3$ | 0.15(5) | – | 0.16(6) | 0.08(3) | – | 0.12(1) | 0.12(6) | – | – | 0.10(4) | 0.10(4) |
| $Cr_2O_3$ | 61.4(6) | 52.9(5) | 53.0(2) | 58.6(3) | 59.8(5) | 59.1(4) | 58.3(3) | 57.7(5) | 60.5(8) | 59.8(3) | 60.0(6) |
| MnO | 0.20(7) | 0.25(3) | 0.21(5) | 0.19(5) | 0.23(7) | 0.22(4) | 0.23(3) | 0.25(4) | 0.24(4) | 0.25(5) | 0.25(3) |
| NiO | 0.10(1) | 0.10(2) | 0.09(2) | 0.12(3) | 0.09(4) | 0.11(3) | 0.17(1) | 0.13(5) | – | – | 0.13(4) |
| $FeO_{tot}$ | 13.4(2) | 17.5(1) | 15.8(2) | 14.4(2) | 14.8(2) | 14.1(1) | 14.4(3) | 15.4(2) | 15.4(3) | 14.9(3) | 14.7(2) |
| FeO* | 6.9(3) | 14.4(2) | 13.0(2) | 8.2(3) | 10.8(2) | 10.3(2) | 11.1(3) | 11.9(2) | 12.0(3) | 11.6(3) | 11.0(3) |
| $Fe_2O_3$* | 7.3(2) | 3.51(8) | 3.17(8) | 6.9(2) | 4.4(1) | 4.23(9) | 3.7(1) | 3.94(9) | 3.8(1) | 3.6(1) | 4.1(1) |
| FeO† | 13.3 | 15.0 | 13.6 | 12.0 | 12.9 | 12.9 | 11.6 | 12.8 | 13.3 | 13.0 | 11.9 |
| $Fe_2O_3$† | 0.1 | 2.8 | 2.5 | 2.6 | 2.1 | 1.4 | 3.1 | 2.9 | 2.4 | 2.1 | 3.2 |
| **Cations on basis of 4 oxygen atoms** | | | | | | | | | | | |
| Zn | – | – | – | – | – | – | – | – | – | – | 0.002(1) |
| Mg | 0.62(1) | 0.584(7) | 0.631(5) | 0.658(8) | 0.641(8) | 0.641(7) | 0.682(4) | 0.647(5) | 0.627(7) | 0.633(5) | 0.668(5) |
| Al | 0.379(5) | 0.554(4) | 0.575(4) | 0.410(3) | 0.402(4) | 0.440(5) | 0.437(4) | 0.452(3) | 0.366(6) | 0.383(4) | 0.376(2) |
| Si | 0.001(1) | – | – | – | – | 0.001(1) | 0.002(1) | – | – | – | 0.001(1) |
| $Ti^{4+}$ | 0.003(1) | 0.005(1) | 0.005(1) | 0.003(1) | 0.005(1) | 0.002(1) | 0.003(1) | 0.003(1) | 0.002(1) | 0.002(1) | 0.003(1) |
| $V^{3+}$ | 0.004(1) | – | 0.004(1) | 0.002(1) | – | 0.003(1) | 0.003(2) | – | – | 0.003(1) | 0.003(1) |
| $Cr^{3+}$ | 1.56(1) | 1.363(8) | 1.346(6) | 1.492(8) | 1.523(8) | 1.500(8) | 1.474(7) | 1.465(8) | 1.56(1) | 1.550(7) | 1.532(9) |
| $Mn^{2+}$ | 0.005(2) | 0.007(1) | 0.006(1) | 0.005(1) | 0.006(2) | 0.006(1) | 0.006(1) | 0.007(1) | 0.007(1) | 0.007(1) | 0.007(1) |
| $Fe^{2+}$ | 0.185(7) | 0.392(4) | 0.349(6) | 0.221(6) | 0.291(6) | 0.276(4) | 0.297(8) | 0.319(4) | 0.329(7) | 0.318(8) | 0.298(7) |
| $Fe^{3+}$ | 0.177(5) | 0.086(2) | 0.077(2) | 0.167(4) | 0.108(3) | 0.102(2) | 0.089(3) | 0.095(2) | 0.093(3) | 0.090(3) | 0.099(3) |
| $Ni^{2+}$ | 0.003(1) | 0.003(1) | 0.002(1) | 0.003(1) | 0.002(1) | 0.003(1) | 0.004(1) | 0.003(1) | – | – | 0.003(1) |
| TOT | 2.935 | 2.993 | 2.994 | 2.962 | 2.978 | 2.974 | 2.995 | 2.991 | 2.987 | 2.985 | 2.991 |
| Vacancy | 0.065 | 0.007 | 0.006 | 0.038 | 0.022 | 0.026 | 0.005 | 0.009 | 0.013 | 0.015 | 0.009 |
| $\Delta Fe^{3+}$‡ | 0.174 | 0.018 | 0.016 | 0.102 | 0.057 | 0.069 | 0.013 | 0.024 | 0.034 | 0.039 | 0.022 |

*Notes:* Digits in brackets: standard deviation (1σ) for both oxides and cations.
* From Mössbauer data.
† From stoichiometry (reported for comparison only, not used for ion calculation).
‡ $\Delta Fe^{3+} = Fe^{3+}_{MS} - Fe^{3+}_{EMPA}$.

which has a low $Cr^{3+}$ content (0.70 apfu) and, conversely, high Al (1.25 apfu), falling within the compositional field of spinel sensu stricto (s.s.). The crystals are thus characterized by $Cr^{3+} \leftrightarrow$ Al substitution along the magnesiochromite–spinel s.s. join.

The contents of $Fe^{3+}$ measured by Mössbauer spectroscopy were always higher than the contents calculated from EMPA on the basis of spinel stoichiometry (Table 4). The difference between measured and calculated $Fe^{3+}$ ($\Delta Fe^{3+}$) is a maximum for crystal Tro6-f (0.17 apfu) but also very significant for Thkv1-a, Thkv1-w, N7-g, Ba2-y, Shb4-b, Shb4-f, and Shb2-m (0.03–0.10 apfu), because it is well beyond the experimental uncertainty (≤0.005 apfu). Because of this excess, chemical formulae of the 17 crystals require cation vacancies to achieve charge-balance (Table 4). However, vacancies were unequivocally observed only in 8 crystals (Thkv1-a, Thkv1-w, N7-g, Ba2-y, Shb4-b, Shb4-f, Shb2-m, and Tro6-f,), because their content was beyond the maximum uncertainty estimated for $Fe^{3+}$ determination. These crystals are therefore non-stoichiometric, a common feature in both naturally and artificially oxidized spinels (Figueiras and Waerenborgh 1997; Menegazzo et al. 1997).

On this basis, it may be assumed that the Albanian crystals underwent oxidation, due to increased environmental oxygen fugacity, after mineral formation. In this view, it is possible to distinguish the $Fe^{2+}$ and $Fe^{3+}$ of primary mineral formation (*P*) from those of subsequent oxidation (*S*). The $Fe^{2+}_P$ and $Fe^{3+}_P$ values may correspond to those calculated from EMPA on a stoichiometric basis. During the oxidation process, $Fe^{3+}_S$ is produced from $Fe^{2+}_P$, and the $Fe^{3+}_S$ values can be calculated as the difference between the $Fe^{3+}$ measured by MS ($Fe^{3+}_{MS}$) and that calculated on a stoichiometric basis: $Fe^{3+}_S = Fe^{3+}_{MS} - Fe^{3+}_P$ (Table 5).

The distribution of Mg, $Fe^{2+}$, $Fe^{3+}$, Al, and cation vacancies (□) in the investigated Cr-spinels is rather complex. The intracrystalline distribution was obtained by an optimization program that minimizes a function, $F(X_i)$, in which both structural and chemical data are taken into account:

$$F(X_i) = \frac{1}{n} \sum_{j=1}^{n} \left( \frac{O_j - C_j(X_i)}{\sigma_j} \right)^2 \quad (1)$$

where $O_j$ is the observed quantity, $\sigma_j$ its standard deviation, $X_i$ the variables, i.e., cation fractions in T and M sites, and $C_j(X_i)$ the same quantity as $O_j$ calculated by means of $X_i$ parameters. The n $O_j$ quantities taken into account were: unit-cell and oxygen parameters; T-O and M-O bond distances; m.a.n. of T and M sites; total atomic proportions given by microprobe analyses; and constraints imposed by crystal chemistry (total charges and occupancies of T and M sites). Several minimization cycles of Equation 1 up to convergence were performed using an in-house calculation routine. Further details about the minimization procedure may be found in Andreozzi et al. (2001). M-O and T-O bond distances were calculated as the linear contribution of each cation multiplied by its specific site bond distance, the latter refined on the basis of analysis of more than 200 spinel structural data from the literature (Lavina et al. 2002). Final cation distributions and $F(X_i)$ values are reported in Table 6.

Results show that the crystals have a normal configuration, due to $Cr^{3+}$ and Al ordered in the M site and Mg and $Fe^{2+}$ in the T site (Table 6). Site distributions obtained for both $Fe^{2+}$ and $Fe^{3+}$ are in agreement with Mössbauer spectroscopy results: octahedrally coordinated $Fe^{3+}$ is higher or close to tetrahedrally coordinated $Fe^{3+}$, except for crystals with high vacancy contents. The substitution $^{M}Cr^{3+} \rightarrow {}^{M}Al$ is responsible for the

**TABLE 4.**—*Extended*

| N2-h | N4-x | N7-g | N10-a | Ba4-c | Ba2-y |
|---|---|---|---|---|---|
| – | – | – | – | – | – |
| 13.3(2) | 17.2(3) | 12.36(8) | 12.1(1) | 14.42(5) | 14.3(2) |
| 10.09(5) | 37.3(6) | 10.19(4) | 9.3(1) | 9.24(6) | 8.91(9) |
| 0.04(2) | – | – | – | 0.04(1) | – |
| 0.09(1) | 0.26(4) | 0.18(2) | 0.12(2) | 0.14(1) | 0.09(2) |
| 0.11(5) | – | – | 0.15(6) | 0.09(1) | 0.11(4) |
| 60.1(4) | 31.2(2) | 57.7(5) | 59.4(4) | 60.2(5) | 63.0(5) |
| 0.22(4) | 0.16(5) | 0.28(6) | 0.27(5) | 0.22(2) | 0.19(5) |
| – | 0.24(7) | 0.11(2) | – | 0.12(3) | 0.12(5) |
| 14.6(4) | 12.6(3) | 16.98(6) | 16.9(3) | 13.47(3) | 11.7(2) |
| | | | | | |
| 12.3(4) | 10.3(3) | 12.4(1) | 13.7(3) | 9.83(8) | 8.0(2) |
| 2.60(9) | 2.51(8) | 5.1(1) | 3.57(9) | 4.04(8) | 4.2(1) |
| 12.8 | 11.2 | 13.9 | 14.4 | 10.7 | 10.9 |
| 2.0 | 1.5 | 3.4 | 2.9 | 3.1 | 0.9 |
| **Cations on basis of 4 oxygen atoms** | | | | | |
| – | – | – | – | – | – |
| 0.647(7) | 0.73(1) | 0.606(4) | 0.597(5) | 0.701(4) | 0.690(8) |
| 0.387(3) | 1.25(1) | 0.395(2) | 0.364(4) | 0.355(3) | 0.340(4) |
| 0.001(1) | – | – | – | 0.001(1) | – |
| 0.002(1) | 0.006(1) | 0.005(1) | 0.003(1) | 0.004(1) | 0.002(1) |
| 0.003(1) | – | – | 0.004(2) | 0.002(1) | 0.003(1) |
| 1.549(9) | 0.701(7) | 1.501(7) | 1.551(7) | 1.552(6) | 1.611(9) |
| 0.006(1) | 0.004(1) | 0.008(2) | 0.008(1) | 0.006(1) | 0.005(1) |
| 0.34(1) | 0.245(7) | 0.341(3) | 0.379(7) | 0.268(2) | 0.216(6) |
| 0.064(2) | 0.054(2) | 0.126(3) | 0.089(2) | 0.099(2) | 0.102(3) |
| – | 0.005(2) | 0.003(1) | – | 0.003(1) | 0.003(1) |
| 2.995 | 2.992 | 2.984 | 2.993 | 2.991 | 2.971 |
| 0.005 | 0.008 | 0.016 | 0.007 | 0.009 | 0.029 |
| 0.014 | 0.021 | 0.041 | 0.018 | 0.023 | 0.078 |

**TABLE 5.** Iron contents (apfu): primary (*P*), from Mössbauer (MS) data, derived by oxidation (*S*)

| | $Fe^{2+}_{P}$ | $Fe^{2+}_{MS}$ | $Fe^{3+}_{P}$ | $Fe^{3+}_{MS}$ | $Fe^{3+}_{S}$ |
|---|---|---|---|---|---|
| Tro6-f | 0.367 | 0.185 | 0.003 | 0.177 | 0.174 |
| Tro4-f | 0.410 | 0.392 | 0.068 | 0.086 | 0.018 |
| Tro4-j | 0.365 | 0.349 | 0.061 | 0.077 | 0.016 |
| Shb2-m | 0.328 | 0.221 | 0.065 | 0.167 | 0.102 |
| Shb4-b | 0.351 | 0.291 | 0.051 | 0.108 | 0.057 |
| Shb4-f | 0.348 | 0.276 | 0.034 | 0.102 | 0.069 |
| Shkm1-i | 0.311 | 0.297 | 0.075 | 0.089 | 0.013 |
| Shkm3-g | 0.344 | 0.319 | 0.071 | 0.095 | 0.024 |
| Thkv1-a | 0.365 | 0.329 | 0.058 | 0.093 | 0.034 |
| Thkv1-w | 0.359 | 0.318 | 0.051 | 0.090 | 0.039 |
| Thkv2-w | 0.322 | 0.298 | 0.077 | 0.099 | 0.022 |
| N2-h | 0.349 | 0.335 | 0.050 | 0.064 | 0.014 |
| N4-x | 0.267 | 0.245 | 0.032 | 0.054 | 0.021 |
| N7-g | 0.384 | 0.341 | 0.085 | 0.126 | 0.041 |
| N10-a | 0.398 | 0.379 | 0.071 | 0.089 | 0.018 |
| Ba4-c | 0.292 | 0.268 | 0.076 | 0.099 | 0.023 |
| Ba2-y | 0.297 | 0.216 | 0.023 | 0.101 | 0.078 |

increase in M-O (1.948–1.982 Å), which influences unit-cell variations (8.274–8.313 Å) to a larger extent than T-O increase (1.957–1.978 Å). It is noteworthy that the temperature-dependent intersite exchange, $^{M}Al + {}^{T}Mg \rightarrow {}^{T}Al + {}^{M}Mg$, commonly observed in spinels, is absent in our crystals. The absence may be due both to the strong stabilization effect of $Cr^{3+}$ for the normal configuration and, presumably, to the low equilibration temperatures (525–730 °C) that the crystals experienced during their cooling history (Beccaluva et al. 1998).

Although cation vacancies were allowed for the T and M sites, the best-optimized site assignments were obtained for vacancies occurring essentially in the T site (Table 6). The same result was obtained by Figueiras and Waerenborgh (1997) for a Portuguese non-stoichiometric chromite, and Chassagneux et al. (1985) for the end-member $(Fe^{3+}_{0.67}\square_{0.33})Cr_2O_4$. This finding indicates that Cr has a strong stabilization effect on tetrahedral vacancies, because both $MgAl_2O_4$ and $Fe_3O_4$ spinels show octahedral vacancies (Lucchesi and Della Giusta 1994; Daniels and Rosencweig 1969). The definition of vacancy distribution in spinels has important implications for the thermodynamic models used to estimate upper mantle $f_{O_2}$. In these models (e.g., Mattioli and Wood 1988, Ghiorso and Sack 1991), only octahedral or randomly distributed vacancies are considered, but these assumptions cannot apply to Cr-spinels, where cation vacancies are essentially located in tetrahedral site.

In our crystals, tetrahedral vacancy content ($^{T}\square$) was directly proportional to $^{T}Fe^{3+}$ in a 1:2 ratio ($r = 0.97$). In turn, $^{T}Fe^{3+}$ showed a strong 1:1 linear correlation ($r = 0.95$) with $Fe^{3+}_{S}$, and this supports their identity. In fact, when plotting oxidized iron $Fe^{3+}_{S}$ vs. $^{T}\square$ values for our crystals, including also the non-stoichiometric chromite of Figueiras and Waerenborgh (1997) and the end-member of Chassagneux et al. (1985), a good correlation, very close to the ratio of 1:2, was observed (Fig. 2). On this basis and considering general oxidation mechanisms (O'Reilly and Banerjee, 1967; Menegazzo et al., 1997), the oxidation process is described by:

$$2\ {}^{T}Fe^{2+} + \tfrac{1}{2}\ O_2 \rightarrow 2\ {}^{T}Fe^{3+} + O^{2-} + {}^{T}\square. \quad (2)$$

thus explaining the observed ratio between $^{T}\square$ and $^{T}Fe^{3+}$.

As evidenced by cation distribution results and Equation 1, chemical replacements in the T site involve $^{T}Mg \leftrightarrow {}^{T}Fe^{2+}$ and $^{T}Fe^{2+}$ oxidation (Fig. 3). Accordingly, T-O variations show a non-linear regression trend with $^{T}Fe^{2+}$, due to the cooperative effects of $^{T}Mg \leftrightarrow {}^{T}Fe^{2+}$ of the above-mentioned substitution and $^{T}Fe^{2+}$ oxidation (Fig. 4).

## PROPERTIES OF CATION VACANCY IN T SITE

In the spinel structure, the isolated T site (8*a* point symmetry) has twelve M sites as a second coordination sphere. A cation vacancy in the T site is thus expected not to impart rigidity to the polyhedron, because it cannot have chemical bonds with ligands: this feature, together with the spinel topology, makes the tetrahedron adopt "soft" behavior. As a consequence, it may be assumed that the $^{T}\square$-O distance does not have a single value,

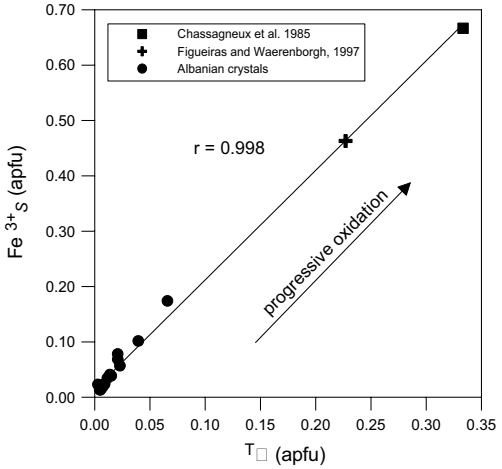


**FIGURE 2.** Oxidized iron ($Fe^{3+}_{S}$) vs. vacancy content in T site ($^{T}\square$). In Albanian crystals, symbol dimensions are proportional to ±2σ.

**TABLE 6.** Final assigned site populations (apfu)

| | Tro6-f | Tro4-f | Tro4-j | Shb2-m | Shb4-b | Shb4-f | Shkm1-i | Shkm3-g | Thkv1-a | Thkv1-w | Thkv2-w | N2-h | N4-x | N7-g | N10-a | Ba4-c | Ba2-y |
|---|---|---|---|---|---|---|---|---|---|---|---|---|---|---|---|---|---|
| **T site** | | | | | | | | | | | | | | | | | |
| Al | 0.001 | 0.010 | 0.007 | 0.000 | 0.006 | 0.000 | 0.016 | 0.001 | 0.000 | 0.017 | 0.000 | 0.010 | 0.064 | 0.001 | 0.002 | 0.005 | 0.013 |
| $Fe^{2+}$ | 0.162 | 0.395 | 0.329 | 0.200 | 0.278 | 0.275 | 0.288 | 0.311 | 0.323 | 0.311 | 0.295 | 0.334 | 0.246 | 0.343 | 0.376 | 0.268 | 0.222 |
| $Fe^{3+}$ | 0.176 | 0.022 | 0.034 | 0.133 | 0.058 | 0.071 | 0.006 | 0.039 | 0.037 | 0.039 | 0.033 | 0.018 | 0.012 | 0.026 | 0.021 | 0.017 | 0.046 |
| Mg | 0.590 | 0.562 | 0.619 | 0.623 | 0.631 | 0.625 | 0.678 | 0.634 | 0.622 | 0.612 | 0.655 | 0.626 | 0.670 | 0.608 | 0.587 | 0.700 | 0.692 |
| $Mn^{2+}$ | 0.003 | 0.007 | 0.006 | 0.004 | 0.006 | 0.006 | 0.006 | 0.007 | 0.007 | 0.006 | 0.007 | 0.006 | 0.004 | 0.009 | 0.008 | 0.006 | 0.006 |
| Si | 0.002 | 0.000 | 0.000 | 0.000 | 0.000 | 0.001 | 0.002 | 0.000 | 0.000 | 0.000 | 0.001 | 0.001 | 0.000 | 0.000 | 0.000 | 0.001 | 0.000 |
| Zn | 0.000 | 0.000 | 0.000 | 0.000 | 0.000 | 0.000 | 0.000 | 0.000 | 0.000 | 0.000 | 0.002 | 0.000 | 0.000 | 0.000 | 0.000 | 0.000 | 0.000 |
| Vacancy | 0.066 | 0.005 | 0.006 | 0.039 | 0.023 | 0.021 | 0.005 | 0.009 | 0.011 | 0.015 | 0.008 | 0.005 | 0.004 | 0.014 | 0.007 | 0.003 | 0.021 |
| Σ T | 1.000 | 1.000 | 1.000 | 1.000 | 1.000 | 1.000 | 1.000 | 1.000 | 1.000 | 1.000 | 1.000 | 1.000 | 1.000 | 1.000 | 1.000 | 1.000 | 1.000 |
| **M site** | | | | | | | | | | | | | | | | | |
| Al | 0.392 | 0.542 | 0.567 | 0.422 | 0.399 | 0.443 | 0.422 | 0.451 | 0.368 | 0.369 | 0.377 | 0.377 | 1.175 | 0.393 | 0.362 | 0.349 | 0.323 |
| $Fe^{2+}$ | 0.000 | 0.000 | 0.021 | 0.000 | 0.010 | 0.000 | 0.007 | 0.007 | 0.007 | 0.002 | 0.000 | 0.001 | 0.005 | 0.000 | 0.002 | 0.001 | 0.001 |
| $Fe^{3+}$ | 0.002 | 0.064 | 0.043 | 0.033 | 0.049 | 0.031 | 0.083 | 0.056 | 0.056 | 0.050 | 0.066 | 0.046 | 0.042 | 0.101 | 0.068 | 0.082 | 0.056 |
| Mg | 0.000 | 0.024 | 0.012 | 0.020 | 0.011 | 0.012 | 0.004 | 0.013 | 0.002 | 0.020 | 0.012 | 0.023 | 0.064 | 0.000 | 0.010 | 0.003 | 0.001 |
| $Cr^{3+}$ | 1.581 | 1.362 | 1.346 | 1.506 | 1.524 | 1.500 | 1.474 | 1.466 | 1.563 | 1.553 | 1.535 | 1.548 | 0.703 | 1.499 | 1.551 | 1.551 | 1.607 |
| $V^{3+}$ | 0.004 | 0.000 | 0.004 | 0.002 | 0.000 | 0.003 | 0.003 | 0.000 | 0.000 | 0.003 | 0.003 | 0.003 | 0.000 | 0.000 | 0.004 | 0.002 | 0.003 |
| $Ni^{2+}$ | 0.003 | 0.003 | 0.002 | 0.003 | 0.002 | 0.003 | 0.004 | 0.003 | 0.000 | 0.000 | 0.003 | 0.000 | 0.005 | 0.003 | 0.000 | 0.003 | 0.003 |
| $Ti^{4+}$ | 0.003 | 0.005 | 0.005 | 0.003 | 0.005 | 0.002 | 0.003 | 0.003 | 0.002 | 0.002 | 0.003 | 0.002 | 0.006 | 0.005 | 0.003 | 0.004 | 0.002 |
| Vacancy | 0.014 | 0.000 | 0.000 | 0.010 | 0.000 | 0.007 | 0.001 | 0.001 | 0.003 | 0.002 | 0.002 | 0.000 | 0.000 | 0.001 | 0.000 | 0.005 | 0.005 |
| Σ M | 2.000 | 2.000 | 2.000 | 1.999 | 2.000 | 2.000 | 2.000 | 2.000 | 2.000 | 2.000 | 2.000 | 2.000 | 2.000 | 2.000 | 2.000 | 2.000 | 2.000 |
| $F(X_i)$ | 3.21 | 0.19 | 0.18 | 5.95 | 0.24 | 0.47 | 0.03 | 0.10 | 0.06 | 0.23 | 0.21 | 0.15 | 0.27 | 0.20 | 0.03 | 0.21 | 0.31 |

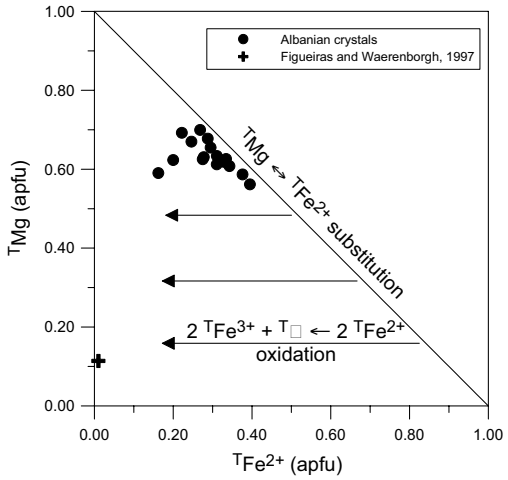


**FIGURE 3.** $^{T}Mg$ vs. $^{T}Fe^{2+}$. Solid line: 1:1 inverse relationship $^{T}Mg \leftrightarrow {}^{T}Fe^{2+}$. Arrows: $^{T}Fe^{2+}$ oxidation process. Symbol dimensions are proportional to ±2σ.

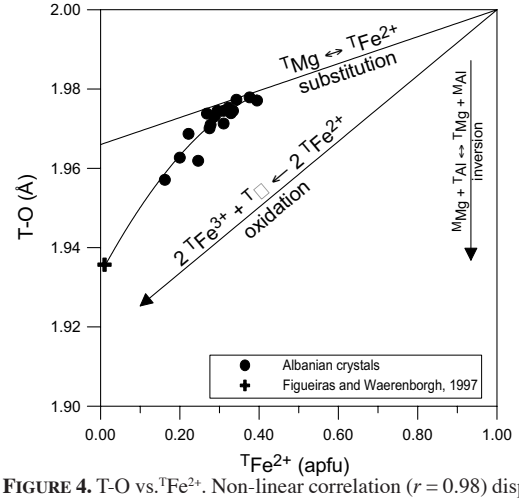


**FIGURE 4.** T-O vs.$^{T}Fe^{2+}$. Non-linear correlation ($r$ = 0.98) displayed by experimental data, due to contributions of both $^{T}Mg \leftrightarrow {}^{T}Fe^{2+}$ substitution and $^{T}Fe^{2+}$ oxidation. Ideal trends were calculated by specific bond distances of Lavina et al. (2002). Influence of Mg ↔ Al inversion is negligible. Symbol dimensions are proportional to ±2σ.

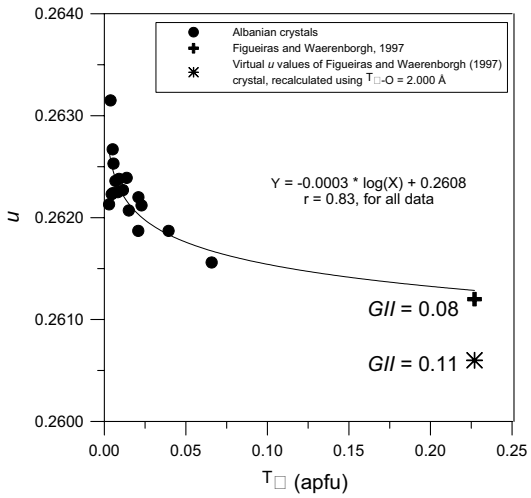


**FIGURE 5.** Semi-logarithmic regression between $u$ and $^{T}□$. Note that $u$ values remain greater than 0.26, which, according to Lavina et al. (2003), is the minimum value observed in normal spinels. The actual *GII* for sample of Figueiras and Waerenborgh (1997) is 0.08 v.u., but it becomes 0.11 v.u. when recalculated using $^{T}□$-O = 2.000 Å. Symbol dimensions are proportional to ±σ.

but changes according to the cation dominating in the M site. This behavior is in good agreement with experimental evidence, because there is a marked difference between the $^{T}□$-O distance used in this work and those used in the literature to optimize site populations. The observed difference is due to the different cations in the M site: $^{T}□$-O = 2.000 Å for our crystals ($^{M}Cr >> {}^{M}Al$), $^{T}□$-O = 2.056 Å for the Al-rich chromite ($^{M}Cr \cong {}^{M}Al$) of Figueiras and Waerenborgh (1997), and $^{T}□$-O = 2.30 Å for end-member maghemite with tetrahedral vacancies (Basso et al. 1991).

Independent confirmation of the need for a "flexible" $^{T}□$-O distance in the spinel structure may be obtained by applying the Bond Valence Model (Brown 2002). This model predicts atomic arrangements and clarifies important structural features such as the presence and extent of strain. Bond valence values, calculated using the equation proposed by Brown and Altermatt (1985), estimate the *global instability index, GII* (Salinas-Sanchez et

al. 1992; Brown 2002), that is, the degree of bond strain in a crystal. Any increase in *GII* to values greater than 0.05 valence units, (v.u.) indicates progressive instability in the structure. In this case, bond distances would be incommensurate under the constraints imposed by crystal geometry, so that the structure tries to relieve the stress introduced by bond distances by stretching or compressing them in order to fit into a particular arrangement.

Of note is the fact that both *GII* values retrieved for our crystals and the Portuguese sample (Figueiras and Waerenborgh 1997) are lower than 0.08 v.u. (Fig. 5). However, when we calculate *GII* for the Portuguese sample using our $^{T}\square$-O distance (2.000 Å), *GII* increases to 0.11 v.u., thus indicating great stress in the structure.

## ACKNOWLEDGMENTS

The authors wish to express their gratitude to R. Carampin, who carried out electron microprobe analyses. G. Walton revised the English text. This research was supported by a MURST grant.

## REFERENCES CITED

Andreozzi, G.B., Lucchesi, S., Skogby, H., and Della Giusta, A. (2001) Compositional dependence of cation distribution in some synthetic $(Mg,Zn)(Al,Fe^{3+})_2O_4$ spinels. European Journal of Mineralogy, 13, 391–402.

Basso, R., Carbonin, S., and Della Giusta, A. (1991) Cation and vacancy distribution in a synthetic defect spinel. Zeitschrift für Kristallographie, 194, 111–119.

Beccaluva, I., Coltorti, M., Ferrini, V., Saccani, E., Siena, F., and Zeda, O. (1998) Petrological modeling of Albanian ophiolites with particular regard to the Bulqiza chromite ore deposits. Periodico di Mineralogia, 67, 7–23.

Brown, I.D. (2002): The chemical bond in inorganic chemistry: the bond valence model. Series: International Union of Crystallography Monographs on Crystallography no. 12, 288 p. Oxford University Press, New York.

Brown, I.D. and Altermatt, D. (1985) Bond-valence parameters obtained from a systematic analysis of the Inorganic Crystal Structure Database. Acta Crystallographica, B41, 244–247.

Chassagneux, F., Rousset, A., and Redoules, J.P. (1985) Elaboration et caractérisation de chromites de fer(III) à structure spinelle lacunaire. Journal Solid State Chemistry, 56, 74–83.

Daniels, J.M. and Rosencweig, A. (1969) Mössbauer spectroscopy of stoichiometric and nonstoichiometric magnetite. Journal of Physics and Chemistry of Solids, 30, 1561–1571.

De Grave, E. and Van Alboom, A. (1991) Evaluation of ferrous and ferric Mössbauer fractions. Physics and Chemistry of Minerals, 18, 337–342.

Della Giusta, A., Carbonin, S., and Ottonello, G. (1996) Temperature-dependent disorder in a natural $Mg\text{-}Al\text{-}Fe^{2+}\text{-}Fe^{3+}$-spinel. Mineralogical Magazine, 60, 603–616.

Dobi, A., Premiti, I., Marto, A., Alliu, I., Shenjtari, A., and Keta, S. (1998) Petrological and geochemical features of the ophiolitic massif of Bulqiza and related chromite mineralization. Periodico di Mineralogia, 67, 25–34.

Figueiras, J. and Waerenborgh, J.C. (1997) Fully oxidized chromite in the Serra Alta (South Portugal) quartzites: chemical and structural characterization and geological implications. Mineralogical Magazine, 61, 627–638.

Ghiorso, M.S. and Sack, R.O. (1991) Thermochemistry of the Oxide Minerals. In D.H. Lindsley, Ed., Oxide Minerals: Petrologic and Magnetic Significance, p. 221–262. Reviews in Mineralogy, Mineralogical Society of America, Washington, D.C.

Hålenius, U., Skogby, H., and Andreozzi, G.B., (2002) Influence of cation distribution on the optical absorption spectra of $Fe^{3+}$-bearing spinel s.s.-hercynite crystals: evidence for electron transition in $^{VI}Fe^{2+}\text{-}^{VI}Fe^{3+}$ clusters. Physics and Chemistry of Minerals, 29, 319–330.

Herd, C.D.K. and Papike, J.J. (1999) Nonstoichiometry in SNC spinels: implications for the determination of oxygen fugacity from phase equilibria. Lunar and Planetary Science XXX, Extended abstract, no. 1973, 15–19/3/1999. Lunar and Planetary Institute, Houston, Texas.

Hill, R.J., Craig, J.R., and Gibbs, G.V. (1979) Systematics of the spinel structure type. Physics and Chemistry of Minerals, 4, 317–340.

Larsson, L., O'Neill H.St.C., and Annersten H. (1994). Crystal chemistry of synthetic hercynite ($FeAl_2O_4$) from XRD structural refinements and Mössbauer spectroscopy. European Journal of Mineralogy 6, 39–51.

Lavina, B., Salviulo, G., and Della Giusta, A. (2002) Cation distribution and structure modeling of spinel solid solutions. Physics and Chemistry of Minerals, 29, 10–18.

Lavina, B, Reznitskii, L.Z., and Bosi F. (2003) Crystal chemistry of some Mg, Cr, V normal spinels from Sludyanka (Lake Baikal, Russia): the influence of $V^{3+}$ on structural stability. Physics and Chemistry of Minerals, 30, 599–605.

Lucchesi, S. and Della Giusta, A. (1994) Crystal chemistry of non-stoichiometric Mg-Al synthetic spinels. Zeitschrift für Kristallographie, 209, 714–719.

Lucchesi, S., Russo, U., and Della Giusta, A. (1997) Crystal chemistry and cation distribution in some Mn-rich natural and synthetic spinels. European Journal of Mineralogy, 9, 31–42.

Martignago, F., Dal Negro, A., and Carbonin, S. (2003) How $Cr^{3+}$ and $Fe^{3+}$ affect Mg–Al order–disorder transformation at high temperature in natural spinels. Physics and Chemistry of Minerals, 30, 401–407.

Mattioli, G.S. and Wood, B.J. (1988) Magnetite activities across the $MgAl_2O_4\text{-}Fe_3O_4$ spinel join, with application to thermobarometric estimates of the upper mantle oxygen fugacity. Contributions to Mineralogy and Petrology, 98, 148–162.

Mekshiqi, N., Neziraj, A., and Hoxha, A. (1998). Petrological and structural characteristics of the Tropoja ultramafic massif and its metallogenic potential. Periodico di Mineralogia, 67, 35–42.

Menagazzo, G., Carbonin S., and Della Giusta, A. (1997). Cation and vacancy distribution in an artificially oxidized natural spinel. Mineralogical Magazine, 61, 441–421.

Nell, J. and Wood, B.J. (1989) Thermodynamic properties in a multicomponent solid solution involving cation disorder: $Fe_3O_4\text{-}MgFe_2O_4\text{-}FeAl_2O_4\text{-}MgAl_2O_4$ spinels. American Mineralogist, 74, 1000–1015.

O'Neill, H.St.C, and Dollase, W.A. (1994): Crystal structures and cation distributions in simple spinels from powder XRD structural refinements: $MgCr_2O_4$, $ZnCr_2O_4$, $Fe_3O_4$ and the temperature dependence of the cation distribution in $ZnAl_2O_4$. Physics and Chemistry of Minerals, 20, 541–555.

O'Neill, H.St.C. and Navrotsky, A. (1983) Simple spinels: crystallographic parameters, cation radii, lattice energies and cation distributions. American Mineralogist, 68, 181–194.

——— (1984) Cation distribution and thermodynamic properties of binary spinel solid solutions. American Mineralogist, 69, 733–753.

O'Neill, H.St.C. and Wall, V.J. (1987) The olivine-orthopyroxene-spinel oxygen geobarometer, the nickel precipitation curve, and the oxygen fugacity of the Earth's upper mantle. Journal of Petrology, 28, 1169–1191.

O'Reilly, W. and Banerjee, S.K. (1967) The mechanism of oxidation in titanomagnetites: a magnetic study. Mineralogical Magazine, 36, 29–37.

Pouchou, J.L. and Pichoir, F. (1984) A new model for quantitative X-ray microanalysis. I. Application to the analysis of homogeneous samples. La Recherche Aérospatiale, 3, 13–36.

Princivalle, F., Della Giusta, A., and Carbonin, S. (1989) Comparative crystal chemistry of spinels from some suites of ultramafic rocks. Mineralogy and Petrology, 40, 117–126.

Sack, R.O. and Ghiorso, M.S. (1991) Chromian spinels as petrogenetic indicators: thermodynamic and petrological applications. American Mineralogist, 76, 827–847.

Salinas-Sanchez, A., Garcia-Muñoz, J.L., Rodriguez-Carvajal, J., Saez-Puche, R., and Martinez, J.L. (1992): Structural characterization of $R_2BaCuO_5$ (R = Y, Lu, Yb, Tm, Er, Ho, Dy, Gd, Eu and Sm) oxides by X-ray and neutron diffraction. Journal Solid State Chemistry, 100, 201–211.

Tokonami, M. and Horiuchi, H. (1980) On the space group of spinel $MgAl_2O_4$. Acta Crystallographica, A36, 122–126.

Waerenborgh, J.C., Annersten, H., Ericsson, T., Figuereido, M.O., and Cabral, J.M.P. (1990) A Mössbauer study of natural gahnite spinels showing strongly temperature dependent quadrupole splitting distributions. European Journal of Mineralogy, 2, 267–271.

Waerenborgh, J.C., Figuereido, M.O., and Cabral, J.M.P. (1994) Powder XRD structure refinements and $^{57}Fe$ Mössbauer effect study of synthetic $Zn_{1-x}Fe_xAl_2O_4$ ($0 < x \leq 1$) spinels annealed at different temperatures. Physics and Chemistry of Minerals, 21, 460–468.

Wood, B.J. (1990) An experimental test of the spinel peridotite oxygen barometer. Journal of Geophysical Research, 95b, 15845–15851.

——— (1991) Oxygen barometry of spinel peridotites. In D.H. Lindsley, Ed., Oxide Minerals: Petrologic and Magnetic Significance. Reviews in Mineralogy, 25, 417–431.

Wood, B.J. and Virgo, D. (1989) Upper mantle oxidation state: ferric iron contents of lherzolite spinels by $^{57}Fe$ Mössbauer spectroscopy and resultant oxygen fugacity. Geochimica Cosmochimica Acta, 53, 1277–1291

MANUSCRIPT RECEIVED OCTOBER 20, 2003
MANUSCRIPT ACCEPTED MARCH 22, 2004
MANUSCRIPT HANDLED BY DARBY DYAR